# An Electromagnetic Calorimeter (BBCal) for the Jefferson Lab Super Bigbite Spectrometer (SBS) Series of Experiments

P. Datta<sup>a,b,\*</sup>, K.T. Evans<sup>c</sup>, S. Abrahamyan<sup>n,d</sup>, J. Bane<sup>l</sup>, H.D. Bhatt<sup>g</sup>, E. Chudakov<sup>d</sup>, B. Devkota<sup>g</sup>, G. Dzyubenko<sup>o</sup>, R. Feuerbach<sup>d,1</sup>, E. Fuchey<sup>a,c</sup>, V. Goryachev<sup>o</sup>, T. Hague<sup>d</sup>, D. Higinbotham<sup>d</sup>, A. Hoebel<sup>d</sup>, M.K. Jones<sup>d</sup>, A. Karki<sup>g</sup>, A. Kollankar<sup>h</sup>, M. Kubantsev<sup>o,m</sup>, S. Li<sup>b</sup>, H. Liu<sup>d</sup>, †C. Long<sup>d</sup>, S. Mayilyan<sup>n</sup>, R. Michaels<sup>d</sup>, D. Nguyen<sup>d</sup>, D. Nikolenko<sup>p</sup>, M. Nycz<sup>k</sup>, R. Pomatsalyuk<sup>q</sup>, A.J.R. Puckett<sup>a</sup>, I. Rachek<sup>p</sup>, B. Reitz<sup>d</sup>, S. Riordan<sup>j</sup>, B. Sawatzky<sup>d</sup>, S. Seeds<sup>a,e</sup>, A. Shahinyan<sup>n</sup>, Y. Shestakov<sup>p</sup>, A. Stepanyan<sup>d</sup>, A.S. Tadepalli<sup>d</sup>, V. Verebryusov<sup>o</sup>, H. Voskanyan<sup>n</sup>, B. Wojtsekhowski<sup>d</sup>, A. Yoon<sup>f,1</sup>

<sup>a</sup>University of Connecticut, Storrs, CT 06269, USA <sup>b</sup>Lawrence Berkeley National Laboratory, Berkeley, CA 94720, USA <sup>c</sup>William & Mary, Williamsburg, VA 23187, USA <sup>d</sup>Thomas Jefferson National Accelerator Facility, Newport News, VA 23606, USA <sup>e</sup>Los Alamos National Laboratory, Los Alamos, NM 87544, USA <sup>f</sup>Christopher Newport University, Newport News, VA 23606, USA <sup>8</sup>Mississippi State University, Mississippi State, MS 39762, USA <sup>h</sup>University of Kentucky, Lexington, KY, USA <sup>i</sup>Temple University, Pennsylvania, PA, USA <sup>j</sup>Carnegie Mellon University, Pittsburgh, PA, USA <sup>k</sup>University of Virginia, Charlottesville, VA, USA <sup>1</sup>University of Massachusets, Amherst, MA, USA <sup>m</sup>Northwestern University, Chicago, IL, USA <sup>n</sup>Yerevan Physics Institute, Yerevan, Armenia <sup>o</sup>Institute of Theoretical and Experimental Physics, Moscow, Russia <sup>p</sup>Budker Institute of Nuclear Physics, Novosibirsk, Russia <sup>q</sup>Kharkov Institute of Physics and Technology, Kharkov, Ukraine

## **Abstract**

We report features of the design, construction, installation, and performance of the lead-glass calorimeter BBCal, constructed as part of the BigBite spectrometer, which served as the electron arm for the Super Bigbite Spectrometer (SBS) program of high-precision neutron electromagnetic form factor measurements in Hall A at Jefferson Lab. As a total-absorption calorimeter, BBCal provided the primary electron trigger for BigBite, detecting (quasi-) elastically scattered electrons in the 1-4 GeV energy range with an energy resolution of approximately 6.2%, position resolution of 1.2 cm, and timing resolution of 0.5 ns.

Keywords: Calorimeter, Shower, Preshower, Nucleon Form Factors

#### 1. Introduction

The first version of the BigBite calorimeter (BBCal) was constructed during the 6 GeV era of Jefferson Lab experiments which were aimed at exploring nucleon form factors in the intermediate  $Q^2$  range [18, 19]. Due to a drop in the cross section at higher  $Q^2$ , the next generation of experiments that wished to extend these form factor measurements required detectors which could handle higher luminosities, requiring higher data acquisition and trigger rate capabilities, and better, radiation-hard calorimeter modules. The advent of high luminosity polarized targets, fast tracking detectors and high intensity electron beams opened doors to a new generation of high precision measurements.

The 12 GeV upgrade of the Continuous Electron Beam Accelerator Facility (CEBAF) [1] has enabled a new generation of

\*Corresponding author

Email address: pdatta@lbl.gov (P. Datta)

high-precision measurements at Jefferson Lab (JLab). Taking advantage of the upgrade to the beam energy and detector capabilities, the Super BigBite Spectrometer (SBS) collaboration conducted a series of experiments in Hall A between fall 2021 and summer 2025 to determine nucleon electromagnetic form factors with unprecedented precision and resolution. The objectives of the experiments that used the calorimeter described in this paper are summarized below:

- E12-09-019 (SBS-GMn, Oct 2021–Feb 2022) First SBS experiment, extending high-precision measurements of the neutron magnetic form factor  $G_M^n$  over  $Q^2 = 3-13.6$   $(\text{GeV}/c)^2$  using the ratio method [22].
- E12-20-010 (SBS-nTPE, Jan 2021–Feb 2022) Ran in series with SBS-GMn to perform the first Rosenbluth separation of the neutron form factors at high  $Q^2$  (~4.5  $(\text{GeV}/c)^2$ ) [21].
- E12-09-016 (GEn-II, Oct 2022-Oct 2023) Extended

Preprint submitted to NIM A November 7, 2025

precision measurements of the neutron electric form factor  $G_E^n$  over  $Q^2 = 3-10 \, (\text{GeV/}c)^2$  via beam–target double spin asymmetry technique utilizing a state-of-the-art polarized <sup>3</sup>He target [10].

- E12-17-004 (GEn-RP, Apr–May 2024) Performed a  $G_E^n$  measurement via the recoil polarization technique at high  $Q^2$  (~4.5 (GeV/c)<sup>2</sup>). Comparison with E12-20-010 results will provide critical tests of the one-photon exchange (OPE) approximation in elastic en scattering [23].
- **E12-20-008** (*K<sub>LL</sub>*, **May 2024**) Performed a measurement of polarization transfer in charged pion photoproduction in the wide angle regime. Data from this experiment will provide a critical test of the applicability of the handbag mechanism [24].

All experiments listed above employed a two-arm coincidence setup. The hadron arm consisted of the Super Bigbite Spectrometer (SBS), while the BigBite Spectrometer (BBS) was used as the electron arm. In the SBS, scattered nucleons were momentum-analyzed by the SBS dipole magnet and detected in a highly segmented hadron calorimeter (HCal) with comparable and high efficiencies for protons and neutrons. The electron arm used the BigBite dipole magnet to bend scattered charged particles into or out of the acceptance depending on their charge and momentum. Precise tracking was achieved with five layers of Gas Electron Multiplier (GEM) detectors, and energy measurements were made in BBCal. Additional BBS subsystems included the Gas Ring Imaging Cherenkov (GRINCH) detector for particle identification and a timing hodoscope for time-of-flight measurements.

The BBS layout is shown in Fig. 1. BBCal—the focus of this work—was designed, constructed, installed, commissioned, and calibrated for the BigBite Spectrometer, and demonstrated reliable performance throughout the SBS program.

## 2. The BigBite Calorimeter

The BigBite calorimeter (BBCal) is a lead glass electromagnetic calorimeter consisting of two parts: the preshower (PS) and shower (SH) layers. Together these layers provide a measurement of the total energy of the scattered electrons. The main purposes of BBCal for each experiment are the following:

- Act as the main experiment trigger,
- Measure the total energy of electrons scattered from the target,
- Identify and differentiate incoming pions and electrons,
- Define a region-of-interest for fast and efficient trackfinding in the GEM system.

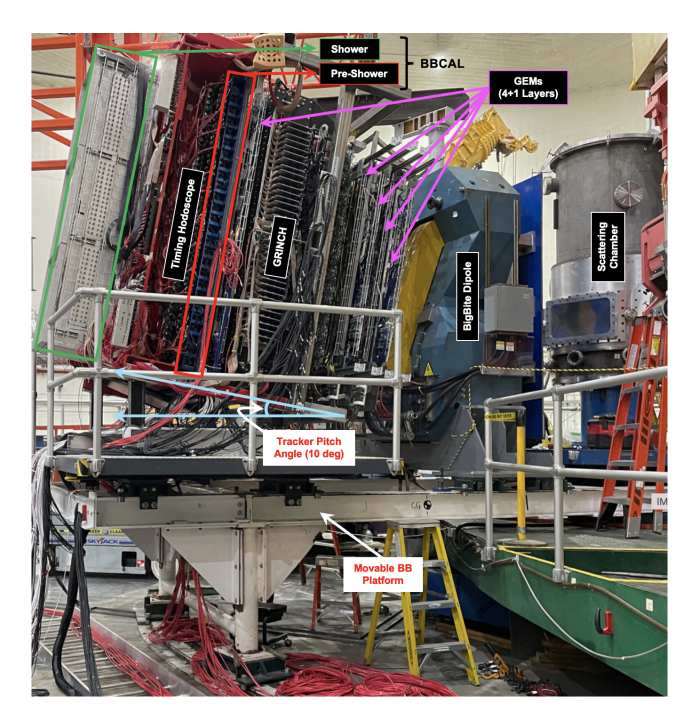


Figure 1: BigBite detector stack installed in experimental Hall A. The scattered electrons emerge from the scattering chamber (right) and pass through the dipole magnet for momentum analysis before entering the detector stack.

#### 2.1. Detector Assembly

#### 2.1.1. Preshower Detector

The PS layer of BBCal was updated from its "old" design used during JLab's 6 GeV era to include new lead glass (LG) blocks (refurbished from the HERMES experiment [7]) for better radiation hardness as well as to implement better magnetic field shielding in the form of mu-metal plates between each row of blocks. The updated PS detector was constructed in the Fall of 2020 at JLab and consists of 52 F101 LG blocks [3], each with dimensions of  $29.5 \times 9 \times 9 \text{ cm}^3$ . Table 1 provides details on the properties of these specific blocks. Each LG block is attached to a Philips XP3461/PA photomultiplier tube (PMT) [4] which reads out the Cherenkov radiation emitted by relativistic charged particles and secondary  $e^+/e^-$  pairs produced in electromagnetic cascades. This combination of LG block and PMT serves as the basic unit of the PS layer. The LG blocks are arranged in 26 rows of two columns oriented perpendicular to the spectrometer axis, with the PMTs connected on the outer edge of each column. As shown in Fig. 2, the PMTs attached to column 0 (1) blocks are on the right (left) side of the PS, when looking downstream.

The PS detector frame is not light-tight because the sides remain open to allow passage for the high voltage and signal readout cables from the PMTs. Thus, before installation, each PS block needed to be individually wrapped in two layers:

- 1. The inner layer is constructed from aluminized mylar, with the mylar side facing inward, making contact with the polished surfaces of the blocks. This layer improves light collection
- 2. The outer layer is constructed from black Tedlar film to provide optical isolation from any stray outside light.

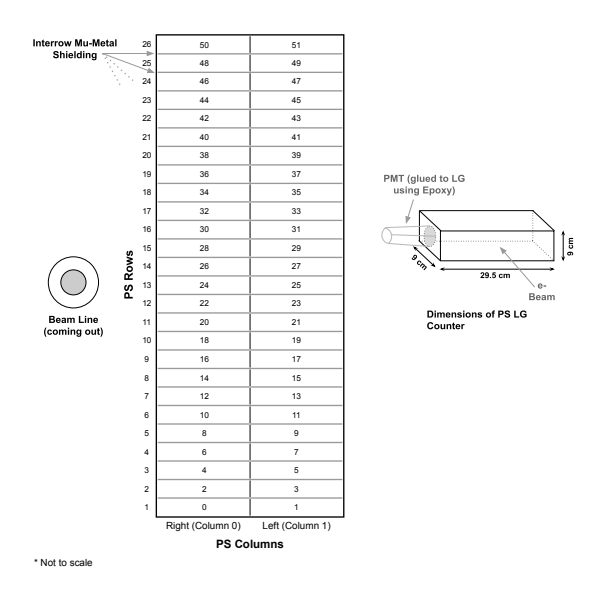


Figure 2: PS detector map (back view).

The orientation of the PS blocks requires scattered particles to traverse approximately 3 radiation lengths (~ 9 cm; see Table 1) of material, which is insufficient to completely stop high-energy electrons. These electrons are subsequently fully absorbed upon passing through the SH blocks. This segmented configuration enables effective electron–pion discrimination. Pions, unlike electrons, interact primarily as minimum ionizing particles (MIPs) within the PS LG, depositing a well-known, low energy of approximately 89 MeV in the PS. This signature is readily identifiable in the PS cluster energy distribution, shown in Fig. 3.

# 2.1.2. Shower Detector

The SH layer was also refurbished since its previous use at JLab. Similar to the PS, each module of the SH consists of one LG block and a corresponding PMT. The SH layer consists of 189 TF1 LG blocks [5][6] each with dimensions of  $8.5 \times 8.5 \times 34 \, \mathrm{cm}^3$ . Table 1 provides details on the properties of the SH blocks. The blocks are stacked in 27 rows of 7 columns which face the incoming scattered particles and are oriented longitudinal to the spectrometer axis, as shown in Fig.

The SH blocks use two types of PMTs: ITEP FEU-110 [2] and Photonis XP5321B [17]. The SH detector frame is light-tight, so the SH blocks are only wrapped in aluminized mylar. Similar to the PS, mu-metal sheets were installed between each row as well as above and below the first and last row (see Fig. 5) in order to provide shielding against stray magnetic fields coming from the SBS and BBS dipole magnets.

The thickness of the SH blocks is 14 radiation lengths. Thus, the PS and SH together constitute approximately 17 radiation lengths, sufficient to fully contain the high-energy electrons of interest.

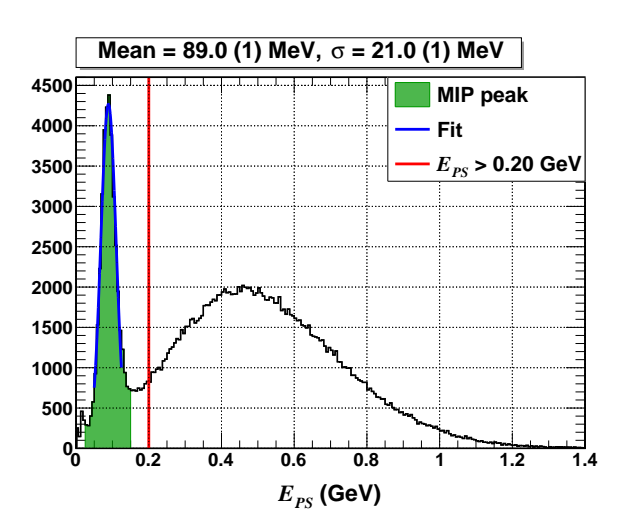


Figure 3: PS cluster energy distribution showing a prominent low-energy peak at approximately 89 MeV, characteristic of MIPs. This feature enables effective rejection of pions from electrons using a simple threshold cut, indicated by the red vertical line. The data shown were obtained at  $Q^2 = 4.5 \, \text{GeV}^2$  with  $E_{\text{beam}} = 4.0 \, \text{GeV}$  during the E12-09-019 experiment and are typical of PS energy spectra obtained throughout the SBS program. For this setting, the scattered electron energies of interest ranged from 1.4-1.9 GeV.

Table 1: Chemical composition and important properties of both types of LG blocks used in BBCal. [8] [9]

F101 (PS)	TF1 (SH)	
Weight (%)		
51.23	0.0	
0.0	51.2	
41.53	41.3	
7.0	7.0	
0.0	0.5	
0.2	0.0	
$3.86  \text{g/cm}^3$	$3.86  \text{g/cm}^3$	
1.65	1.65	
2.78 cm	2.50 cm	
3.28 cm	3.50 cm	
17.97 MeV	15.00 MeV	
	Weight 51.23 0.0 41.53 7.0 0.0 0.2 3.86 g/cm <sup>3</sup> 1.65 2.78 cm 3.28 cm	

# 3. Trigger and Data Acquisition

BBCal was used to define the electron trigger for all the SBS experiments except E12-07-109. The raw PMT signals from the PS and SH layers were amplified and split within the front-end (FE) electronics. One copy of the signals was sent to a flash analog-to-digital converter (fADC) for data acquisition [16], and the other was used to form the electron trigger. The copies of PS and SH signals took slightly different paths through the FE electronics as described below, see Fig. 6.

Raw PMT signals from the PS were first sent to a 2-output 10x Phillips Scientific (PhSc) amplifier model 776. The two amplified output copies were then processed separately:

 One copy was sent directly to a fADC 250 module for digitization.

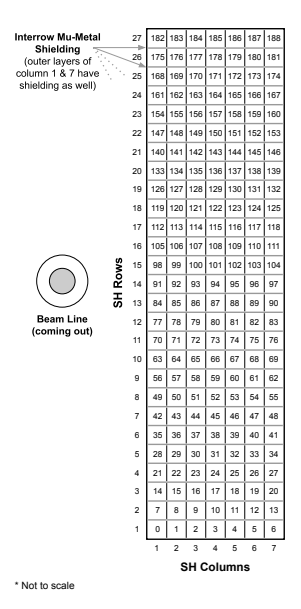




Figure 4: SH detector map (back view).



Figure 5: Sheets of mu metal installed between each row of SH PMTs. This image is from the back of the SH layer during construction.

2. The other was sent to a custom-made 2-output splitter module from which two identical outputs were generated, each amplified by a factor of approximately five. These outputs were then routed into a linear fan-in/fan-out (LFI/O) module to sum signals from overlapping PS rows. These sums were finally sent to PhSc model 740 quad LFI/O modules for final trigger formation.

Raw PMT signals from the SH were sent directly to custom-made Summer/Amplifier (S/A) modules and were split into two copies:

- 1. One copy was amplified by a factor of approximately five before being sent directly to a fADC 250 module for digitization
- The other copy was amplified by a factor of approximately
   3.5 and was summed with amplified signals from the other six SH PMTs in the same row on the calorimeter. The summed output was then sent to the same PhSc model 740

quad LFI/O modules as the PS sums for final trigger formation.

## 3.1. Trigger Sums

In the LFI/O modules where both SH and PS signals were sent, the signals were combined into 25 trigger sums (labeled SC1-2, SC2-3, etc.) each comprising both SH and PS signals, as shown in Table 2. The inclusion of three SH rows instead of two in the eleven trigger sums formed by the middle rows of the SH and PS gives more weight to the events generated within the experimental acceptance. Additionally, such a design accounts for the slight mismatch in geometric alignment between SH rows and their corresponding PS rows.

Table 2: List of BigBite trigger sums formed by the SH and PS rows. Here, PS-1, PS-2, etc. represent the sums of the amplified signals coming from the left and right modules on the PS layer, and SH-1, SH-2, etc. represent the sums of the amplified signals coming from all the seven modules in one SH layer. SC 1-2, SC 2-3, etc. simply represent the different sums from corresponding PS and SH rows.

Trigger Sums         Associated SH & PS Rows           SC 1-2         SH-1 + SH-2 + PS-1 + PS-2           SC 2-3         SH-2 + SH-3 + PS-2 + PS-3           SC 3-4         SH-3 + SH-4 + PS-3 + PS-4           SC 4-5         SH-4 + SH-5 + PS-4 + PS-5           SC 5-6         SH-5 + SH-6 + PS-5 + PS-6           SC 6-7         SH-6 + SH-7 + PS-6 + PS-7           SC 7-8         SH-7 + SH-8 + PS-7 + PS-8           SC 8-9         SH-8 + SH-9 + SH-10 + PS-8 + PS-9           SC 9-10         SH-9 + SH-10 + SH-11 + PS-9 + PS-10           SC 10-11         SH-10 + SH-11 + SH-12 + PS-10 + PS-11           SC 11-12         SH-11 + SH-12 + SH-13 + PS-11 + PS-12           SC 12-13         SH-12 + SH-13 + SH-14 + PS-12 + PS-13           SC 13-14         SH-13 + SH-14 + SH-15 + PS-13 + PS-14
SC 2-3 SH-2 + SH-3 + PS-2 + PS-3 SC 3-4 SH-3 + SH-4 + PS-3 + PS-4 SC 4-5 SH-4 + SH-5 + PS-4 + PS-5 SC 5-6 SH-5 + SH-6 + PS-5 + PS-6 SC 6-7 SH-6 + SH-7 + PS-6 + PS-7 SC 7-8 SH-7 + SH-8 + PS-7 + PS-8 SC 8-9 SH-8 + SH-9 + SH-10 + PS-8 + PS-9 SC 9-10 SH-9 + SH-10 + SH-11 + PS-9 + PS-10 SC 10-11 SH-10 + SH-11 + SH-12 + PS-10 + PS-11 SC 11-12 SH-11 + SH-12 + SH-13 + PS-11 + PS-12 SC 12-13 SH-12 + SH-13 + SH-14 + PS-12 + PS-13
SC 3-4 SH-3 + SH-4 + PS-3 + PS-4 SC 4-5 SH-4 + SH-5 + PS-4 + PS-5 SC 5-6 SH-5 + SH-6 + PS-5 + PS-6 SC 6-7 SH-6 + SH-7 + PS-6 + PS-7 SC 7-8 SH-7 + SH-8 + PS-7 + PS-8 SC 8-9 SH-8 + SH-9 + SH-10 + PS-8 + PS-9 SC 9-10 SH-9 + SH-10 + SH-11 + PS-9 + PS-10 SC 10-11 SH-10 + SH-11 + SH-12 + PS-10 + PS-11 SC 11-12 SH-11 + SH-12 + SH-13 + PS-11 + PS-12 SC 12-13 SH-12 + SH-13 + SH-14 + PS-12 + PS-13
SC 4-5 SH-4 + SH-5 + PS-4 + PS-5 SC 5-6 SH-5 + SH-6 + PS-5 + PS-6 SC 6-7 SH-6 + SH-7 + PS-6 + PS-7 SC 7-8 SH-7 + SH-8 + PS-7 + PS-8 SC 8-9 SH-8 + SH-9 + SH-10 + PS-8 + PS-9 SC 9-10 SH-9 + SH-10 + SH-11 + PS-9 + PS-10 SC 10-11 SH-10 + SH-11 + SH-12 + PS-10 + PS-11 SC 11-12 SH-11 + SH-12 + SH-13 + PS-11 + PS-12 SC 12-13 SH-12 + SH-13 + SH-14 + PS-12 + PS-13
SC 5-6       SH-5 + SH-6 + PS-5 + PS-6         SC 6-7       SH-6 + SH-7 + PS-6 + PS-7         SC 7-8       SH-7 + SH-8 + PS-7 + PS-8         SC 8-9       SH-8 + SH-9 + SH-10 + PS-8 + PS-9         SC 9-10       SH-9 + SH-10 + SH-11 + PS-9 + PS-10         SC 10-11       SH-10 + SH-11 + SH-12 + PS-10 + PS-11         SC 11-12       SH-11 + SH-12 + SH-13 + PS-11 + PS-12         SC 12-13       SH-12 + SH-13 + SH-14 + PS-12 + PS-13
SC 6-7       SH-6 + SH-7 + PS-6 + PS-7         SC 7-8       SH-7 + SH-8 + PS-7 + PS-8         SC 8-9       SH-8 + SH-9 + SH-10 + PS-8 + PS-9         SC 9-10       SH-9 + SH-10 + SH-11 + PS-9 + PS-10         SC 10-11       SH-10 + SH-11 + SH-12 + PS-10 + PS-11         SC 11-12       SH-11 + SH-12 + SH-13 + PS-11 + PS-12         SC 12-13       SH-12 + SH-13 + SH-14 + PS-12 + PS-13
SC 7-8       SH-7 + SH-8 + PS-7 + PS-8         SC 8-9       SH-8 + SH-9 + SH-10 + PS-8 + PS-9         SC 9-10       SH-9 + SH-10 + SH-11 + PS-9 + PS-10         SC 10-11       SH-10 + SH-11 + SH-12 + PS-10 + PS-11         SC 11-12       SH-11 + SH-12 + SH-13 + PS-11 + PS-12         SC 12-13       SH-12 + SH-13 + SH-14 + PS-12 + PS-13
SC 8-9       SH-8 + SH-9 + SH-10 + PS-8 + PS-9         SC 9-10       SH-9 + SH-10 + SH-11 + PS-9 + PS-10         SC 10-11       SH-10 + SH-11 + SH-12 + PS-10 + PS-11         SC 11-12       SH-11 + SH-12 + SH-13 + PS-11 + PS-12         SC 12-13       SH-12 + SH-13 + SH-14 + PS-12 + PS-13
SC 9-10       SH-9 + SH-10 + SH-11 + PS-9 + PS-10         SC 10-11       SH-10 + SH-11 + SH-12 + PS-10 + PS-11         SC 11-12       SH-11 + SH-12 + SH-13 + PS-11 + PS-12         SC 12-13       SH-12 + SH-13 + SH-14 + PS-12 + PS-13
SC 10-11 SH-10 + SH-11 + SH-12 + PS-10 + PS-11 SC 11-12 SH-11 + SH-12 + SH-13 + PS-11 + PS-12 SC 12-13 SH-12 + SH-13 + SH-14 + PS-12 + PS-13
SC 11-12 SH-11 + SH-12 + SH-13 + PS-11 + PS-12 SC 12-13 SH-12 + SH-13 + SH-14 + PS-12 + PS-13
SC 12-13 SH-12 + SH-13 + SH-14 + PS-12 + PS-13
SC 13-14 SH-13 + SH-14 + SH-15 + PS-13 + PS-14
SC 14-15 SH-14 + SH-15 + SH-16 + PS-14 + PS-15
SC 15-16 SH-15 + SH-16 + SH-17 + PS-15 + PS-16
SC 16-17 SH-16 + SH-17 + SH-18 + PS-16 + PS-17
SC 17-18 SH-17 + SH-18 + SH-19 + PS-17 + PS-18
SC 18-19 SH-18 + SH-19 + SH-20 + PS-18 + PS-19
SC 19-20 SH-20 + SH-21 + PS-19 + PS-20
SC 20-21 SH-21 + SH-22 + PS-20 + PS-21
SC 21-22 SH-22 + SH-23 + PS-21 + PS-22
SC 22-23 SH-23 + SH-24 + PS-22 + PS-23
SC 23-24 SH-24 + SH-25 + PS-23 + PS-24
SC 24-25 SH-25 + SH-26 + PS-24 + PS-25
SC 25-26 SH-26 + SH-27 + PS-25 + PS-26

Two of the outputs from the quad LFI/O were used for the following purpose:

- 1. One output was sent directly to a fADC 250 module as part of the trigger performance monitoring system.
- 2. The other output was used to form the main electron trigger.

Each of these final LFI/O outputs were filtered using a highpass filter to get rid of any DC offsets and baseline fluctuations. Fig. 7 shows a diagram of the filter that was used for each output.

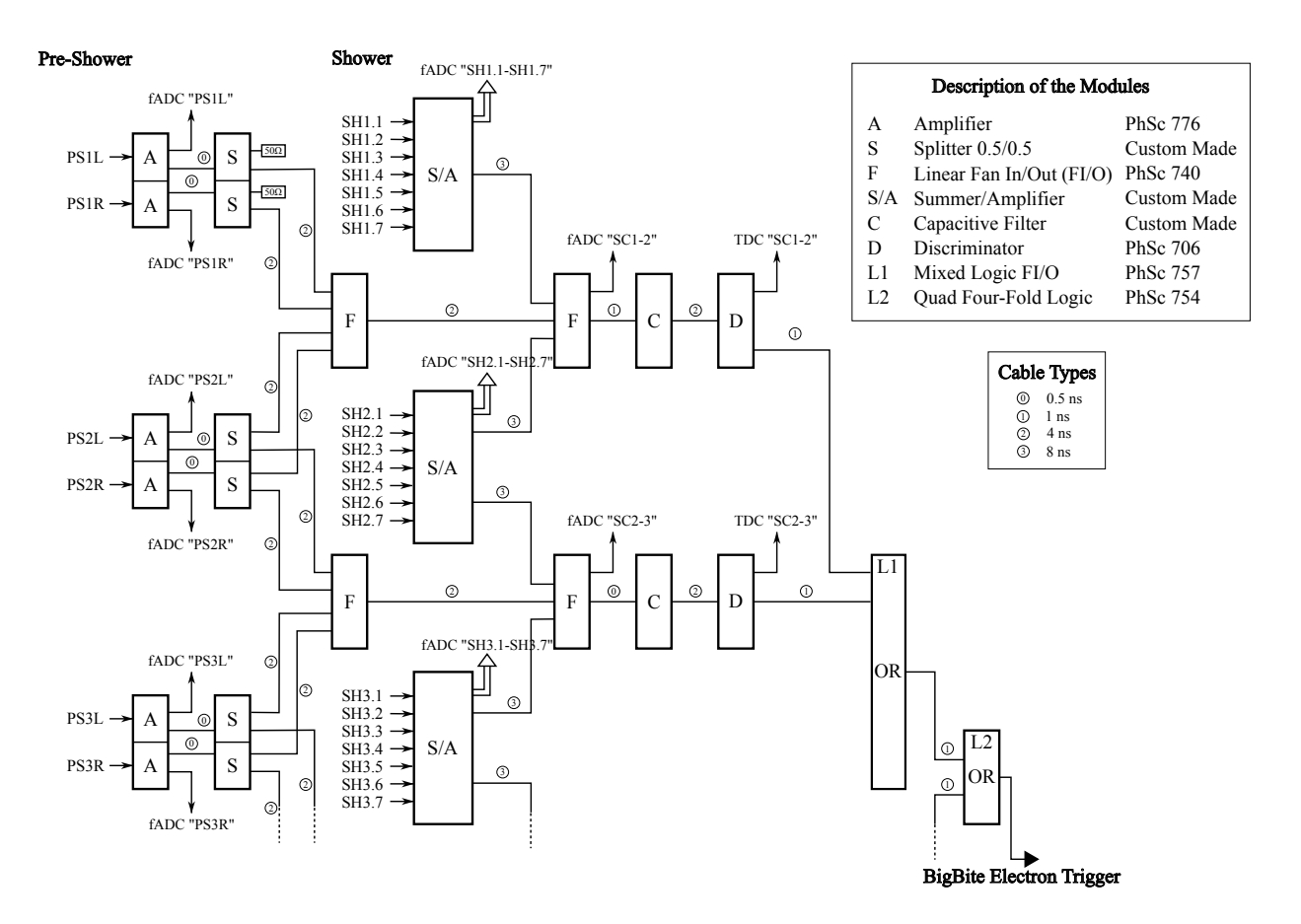


Figure 6: Schematic of a subset of the FE electronics. [14]

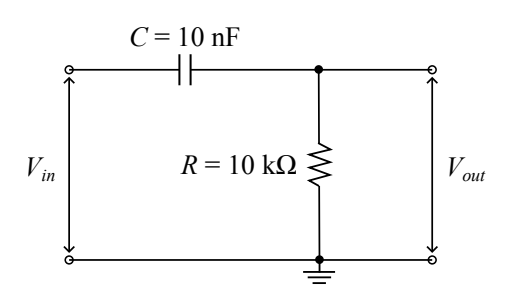


Figure 7: Circuit diagram of the high-pass filter in the BBCal trigger circuit.

The filtered trigger sums were then processed by PhSc model 706 discriminators which were modified to allow remote threshold adjustment. The output pulse widths of the discriminators were kept constant at 40 ns throughout all the experiments.

# 3.2. Threshold Determination

An optimal remotely adjustable threshold on the BBCal trigger was chosen such that the DAQ live time was maximized while the loss of physics events of interest was minimized.

The minimum expected scattered electron energy for each experimental kinematic configuration was determined via real-

istic simulation (see Sec. 7), and this value was used to place the threshold such that scattered electrons above this energy were recorded. However, in order to convert the energy (in MeV) to the threshold setting (in mV) at the discriminator level, we determined a threshold conversion factor,  $Th_{CF}$ , which is found by

$$Th_{CF} = C \times A_{Trig} \tag{1}$$

where  $A_{Trig}$  is the signal amplitude in units of mV at the trigger level<sup>1</sup> after cosmic calibrations (see Sec. 5.1) and C is a constant in units of MeV<sup>-1</sup>. Table 3 shows the conversion factors found for different kinematic settings during E12-09-019. An initial empirical value for C was estimated using the known cosmic energy deposition per BBCal block, 72 MeV (see Sec. 5.1). Later, the value was fine tuned by comparing with the leading edge of the BBCal cluster energy distribution obtained from hydrogen data.

We chose  $A_{Trig}$  during calibrations based on the saturation level of the trigger electronics, specifically the saturation level of the S/A modules which is 200 mV. The saturation value of the S/A modules was carefully determined to be the controlling factor in the saturation of our circuit. We use this saturation

<sup>&</sup>lt;sup>1</sup>Trigger level here means the signal at the input of the quad LFI/O where the trigger sums are made.

Table 3: Scattered electron energy $(E'_E)$ , 4-momentum transfer $(Q^2)$ ,	beam energy ( $E_{\text{beam}}$ ), and threshold conversion factor ( $Th_{CF}$ ) for different E12-09-019
kinematic configurations.	

Central $E'_e$ (GeV)	Minimum $E'_e$ (GeV)	Maximum $E'_e$ (GeV)	$Q^2 (\text{GeV/c})^2$	E <sub>beam</sub> (GeV)	Th <sub>CF</sub> (mV/MeV)
1.6	1.43	1.86	4.5	4.0	0.44
2.0	1.75	2.31	7.4	6.0	0.35
2.1	1.88	2.39	3.0	3.7	0.35
2.7	2.27	3.15	9.9	7.9	0.26
2.7	2.29	3.25	13.6	9.9	0.26
3.6	3.09	4.14	4.5	6.0	0.18

value along with the maximum expected scattered electron energy from simulation,  $E_e^{Max}$ , to calculate an upper bound on our  $A_{Trig}$  value:

$$A_{Trig}^{Max} \le C_{elec} \times \frac{E_{dep}^{cos}}{E_{e}^{Max}} \times 200 \text{mV}$$
 (2)

where  $C_{elec}$  is the factor due to the combined contributions of amplification and signal attenuation within our electronics, and  $E_{dep}^{cos}$  is the total average energy deposited in a LG block by a cosmic ray.

Once Eqn (2) was used to determine a maximum value for our  $A_{Trig}$  setting, this value was then used along with Eqn (1) to calculate the threshold conversion factor. As an example, in E12-09-019, the  $Q^2 = 4.5 \text{ (GeV/c)}^2$  kinematic configuration had an  $A_{Trig}^{Max}$  of 10 mV and a  $Th_{CF}$  of 0.18 mV/MeV.

## 3.3. Signal Amplitude Mapping

In order for the electron trigger to be stable and efficient, the PMT signal amplitudes needed to be matched at the trigger level, despite only having the ability to read the fADC signals using our DAQ system. Due to differences in amplification and attenuation between the two PMT signal copies which were split at the FE, there was a clear discrepancy between the signal amplitude at the trigger level and at the fADCs. Thus, it was vital to establish a map between these two signals.

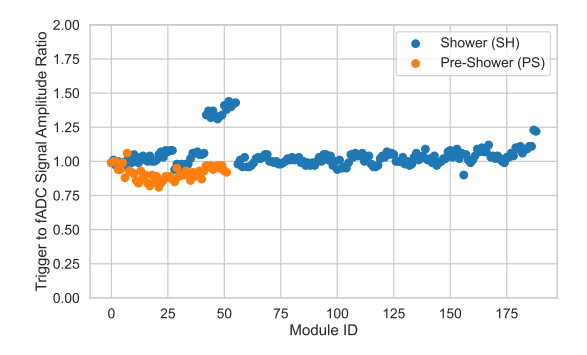


Figure 8: Ratios of signal amplitudes at the trigger over those at the fADC for all BBCal modules. Orange data points represent PS ratios, and blue points represent SH ratios.

A mapping needed to be defined for each channel in order to account for the gain variation across the S/A modules. A procedure was developed to give pulses with known amplitudes as an

input to each S/A module and record the resulting signal amplitude as an output at the trigger level with an oscilloscope. Then, the corresponding signal was recorded at the fADC. These two signals were compared, and ratios were made for each channel which constitute the mapping between trigger level and fADC. As can be seen in Fig. 8 the ratios were approximately equal to 1 for almost all of the modules, but some channels saw a significant difference in the signals which was properly accounted for by applying these ratios. Thus, the mapping was used to match signal amplitudes at the trigger level.

#### 3.4. High Voltage Monitoring

The High Voltage (HV) distribution system for the BBCal PMTs was comprised of two LeCroy 1458 HV crates with built-in Raspberry Pi (RPI)-based software controls and 21 LeCroy 1461N HV cards. The HV crates were installed in a rack, one on top of the other, in a shielded bunker in the experimental hall to avoid radiation damage during data taking. Each LeCroy 1458 HV crate can hold 16 type 1461N HV cards, each equipped with twelve HV supply channels. Such a design necessitates a total of twenty-one HV cards to be installed in two HV crates to accommodate all 241 BBCal PMTs.

The RPIs allow remote modifications to the HV settings of each individual channel by connecting to Jefferson Lab's EPICS, Experimental Physics Industrial Control System [13], and saving the readouts to an archive. This system also includes online monitoring of voltage and current read-backs for each PMT channel, and trip limits can be set that will alarm when exceeded. The ability to quickly and remotely monitor and modify the HV values was vital for all relevant experiments.

## 4. Clustering Algorithm

A BBCal cluster is a combination of SH cluster and corresponding PS cluster. A clustering algorithm is used to define SH and PS clusters with energy, position, and timing criteria. The total energy deposition in these BBCal clusters is a measure of the scattered electron energy.

Clusters encompass the entire EM shower, and multiple criteria help ensure that each cluster contains only one scattered electron event and that we select the "best" cluster for analysis. For each triggered event, all hits that pass a minimum energy threshold are added to arrays for the SH and PS which stores the position, time, energy, and block index of each hit, and these hits are then ordered in descending energy.

#### 4.1. SH Clusters

The first block in the SH hit array corresponds to the block with the highest energy hit for a given event and is used as the seed for a cluster. The cluster is then made using an "island" clustering algorithm in which blocks are added to the cluster after passing certain criteria when compared to the cluster seed, and the cluster is allowed to grow in any direction, as discussed in the following.

Once a cluster seed is defined, it is added to a new cluster array. Any block added to a cluster array is then deleted from the overall hit array in order to avoid double counting. Starting with the seed block, remaining blocks in the "unused" hit array ("unused" meaning "not yet added to any existing cluster") are compared one-by-one to all blocks that have already been added to the cluster in terms of the following quantities:

$$r_{ii}^2 \equiv (x_i - x_j)^2 + (y_i - y_j)^2$$
,  $t_j \equiv |t_i^{ADC} - t_0^{ADC}|$ ,

where  $(x_i, y_i)$  and  $(x_j, y_j)$  are, respectively, the center coordinates of the ith block already added to the cluster and the jth unused block.  $t_j^{ADC}$  and  $t_0^{ADC}$  are, respectively, the ADC times (see section 6) of the jth block and the "seed" block. In order for a block to be added to the cluster array, the following criteria must be met:

$$r_{ii}^2 \le r_{max}^2 \quad , \quad t_j \le t_{max} \tag{3}$$

In other words, as blocks are added to the cluster and removed from the "unused blocks" array, remaining unused blocks are compared to every block that has been previously added to the cluster, and if an unused block is within a radius  $r_{max}$  of any block already in the cluster and "in-time" with the seed block (which generally has the best timing resolution), it is added to the cluster. This process continues until no more neighboring blocks are found satisfying the squared-distance and time criteria of equation (3). In this way, clusters are allowed to grow to arbitrary size in any direction, essentially grouping all contiguous blocks whose hits are sufficiently close in time to the seed.

For E12-09-019,  $r_{max}$  was defined as 15 cm. Given the shower block size and layout, this value accommodates nearest horizontal, vertical, and diagonal neighbors.  $t_{max}$  was conservatively chosen to be 10 ns, and the rationale for this choice is described in more detail in Section 6. Finally, the total energy of the SH cluster must pass a minimum energy threshold in order to be added to an array of clusters for each event. Typical SH cluster multiplicities are shown in Fig. 10a.

### 4.2. PS Clusters

For each SH cluster, a corresponding PS cluster is defined. Similar to the method of creating SH clusters, we start with a hit array on the PS for a given triggered event. The energy-weighted centroid position of the SH cluster is projected onto the PS layer, and the center of each PS block is compared to this. If the vertical (horizontal) distances between this centroid position and a given block position is less than 15 (20) cm, then the PS block passes the position criterion. The PS block in

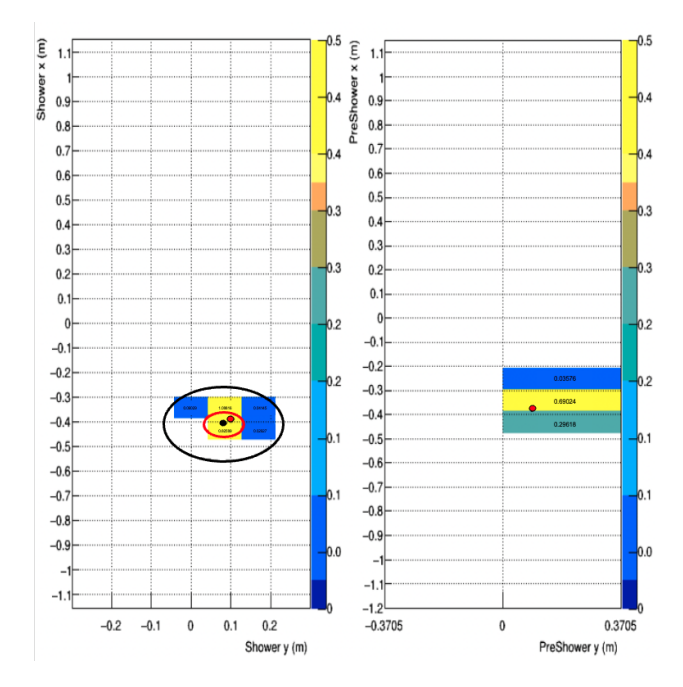


Figure 9: Visualization of the highest-energy BBCal cluster for an example event from E12-09-019. In both plots, the color scale indicates the energy deposited in each block. Colored blocks correspond to those passing the position, time, and energy criteria of the clustering algorithm. In the left plot, the larger black ellipse marks the BBCal clustering search region, while the smaller red ellipse denotes the tracking system's search region. The black filled circle indicates the SH cluster centroid, and the red filled circles represent the reconstructed electron track positions projected onto SH (left) and PS (right).

which the projected SH cluster position lies is the seed block of the PS cluster.

The ADC time of each PS block is also compared to the ADC time of the SH cluster, and if the difference in these times is less than 10 ns then the PS block passes the timing criterion and is added to the PS cluster. Once a block is added to a cluster, it is removed from the overall hit array. Typical PS cluster multiplicity is shown in Fig. 10b.

## 4.3. Best Cluster Selection

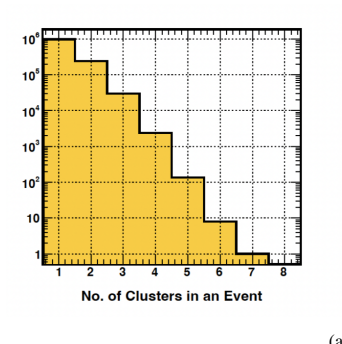
We define the "best" cluster as that which correlates with the event with the highest *total* combined PS and SH energy. Fig. 9 shows an example of the best SH cluster and corresponding PS cluster for a given event.

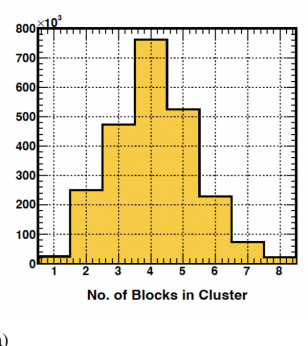
# 5. Energy Calibration

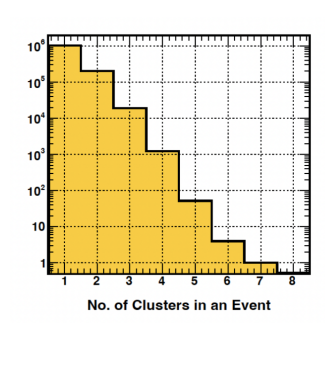
Initial energy calibrations for the calorimeter were performed using cosmic ray data at the beginning of every experimental configuration. Later, a more sophisticated method was used to fine tune the energy calibration coefficients using data from scattering of electrons on hydrogen.

#### 5.1. Cosmic Ray Calibrations

Due to their nature as MIPs, cosmic-ray muons deposit a relatively small and well-defined amount of energy in the calorimeter's lead-glass blocks. For a single vertical muon







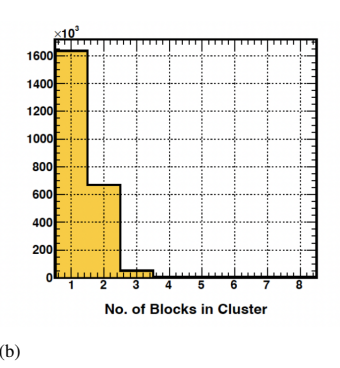


Figure 10: Cluster multiplicity and size distributions for SH (a) and PS (b). The data shown were obtained from quasi-elastic scattering events with a deuterium target during E12-09-019 at  $Q^2 = 13.6 \text{ GeV}^2$  with  $E_{\text{beam}} = 9.9 \text{ GeV}$ . For this setting, the scattered electron energies of interest ranged from 3.09-4.14 GeV.

traversing one block (in either the SH or PS), the total energy deposition is approximately 72 MeV<sup>2</sup>.

Our initial energy calibration exploited this feature to equalize the ADC response across blocks by adjusting the PMT high voltages, thereby gain-matching the PMTs. To ensure a uniform calibration sample, only vertical cosmic rays were selected. The event selection imposed a "verticality cut," defined as follows:

- For the SH, an event was accepted if the four vertical neighbors of a given block (the two above and two below) showed good signals, while its two horizontal neighbors did not exceed threshold.
- For the PS, an analogous cut was applied, requiring good signals only in the four vertical neighbors.

After applying this selection, signal amplitude distributions were fitted to extract peak positions. These peak values were then aligned to a common reference by adjusting the PMT high voltages.

$$HV_{new} = HV_{old} \left( \frac{A_{Trig}^{set}}{V_{old}} \right)^{\frac{1}{\alpha}}$$
 (4)

where:

 $\alpha \equiv PMT$  gain factor

 $HV_{old} \equiv PMT HV$  before calibration

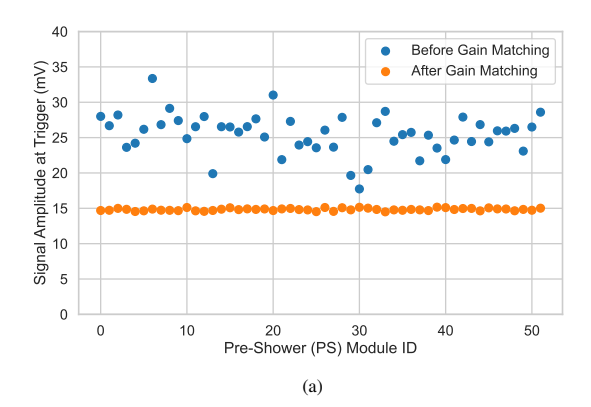
 $HV_{new} \equiv$  desired calibrated PMT HV value

 $V_{old} \equiv \text{signal amplitude before calibration}$ 

 $A_{Trig}^{set} \equiv$  desired signal amplitude after calibration (see Sec. 3.2)

The effect of this gain-matching using cosmic data can be seen in Fig. 11.

We carried out several HV scans to determine best value for  $\alpha$ , or the gain factor, for each PMT. This involved taking cosmic



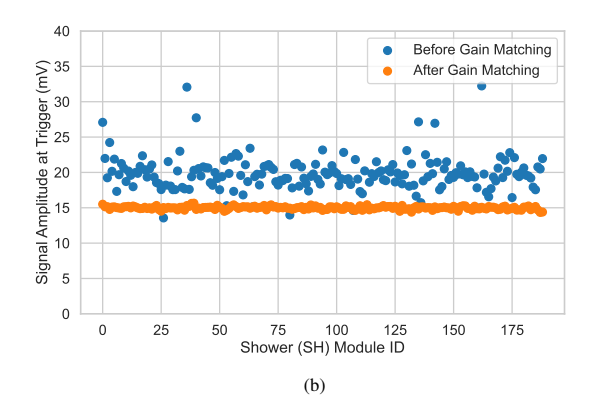


Figure 11: Effect of gain-matching on signal amplitudes for PS (a) and SH (b) blocks. Blue points represent amplitudes before gain-matching, and orange points represent amplitudes after gain-matching.

data using several HV settings to encompass the entire operational range of the PMTs. Then, the plot of peak position vs HV for each PMT was fit using a function of the same form as Eqn (4), and this fit was used to extract the corresponding  $\alpha$ , as shown in Fig. 12. The  $\alpha$  parameters remained the same for all of the PMTs throughout E12-09-019 and E12-09-016, but they were updated before E12-17-004 to account for some deteriorating PMT performance.

<sup>&</sup>lt;sup>2</sup>This value was determined empirically from BBCal cosmic data.

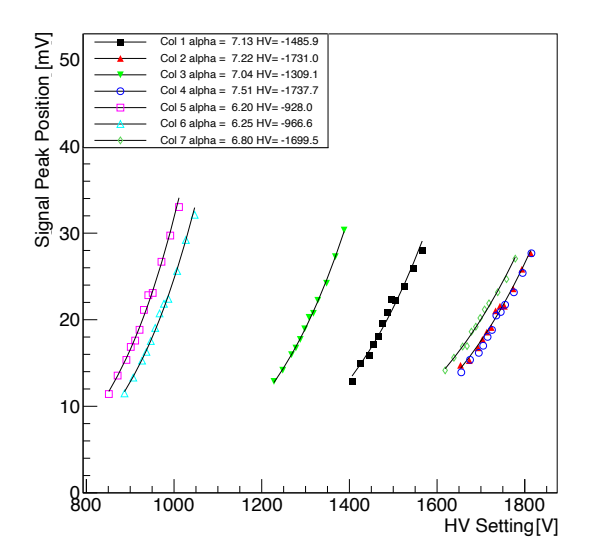


Figure 12: Example plot of a HV scan done in January 2024. The channels plotted are for the seven PMTs in SH row 4, and the HV settings were shifted  $\pm 50~\rm V$  in increments of 10 V from the channels' nominal HV settings. The legend lists the  $\alpha$  values found from the fit, of the form Eqn. 4, and the nominal HV settings in V of the fit for each PMT in SH row 4.

## 5.1.1. Magnetic Field Mitigation

Calibration of the electron trigger critically depends on precise gain-matching of the BBCal photomultiplier tubes (PMTs). Instabilities in the PMT gains can adversely affect the calibration, resulting in a biased and less efficient electron trigger. During the commissioning of the E12-09-019 experiment, a gain instability was observed in the PMTs. This effect was traced to an unexpectedly large fringe magnetic field from the nearby SBS magnet, in addition to a smaller contribution from the BBS magnet. Figure 13 illustrates the impact of these gain variations on the PS and SH signal amplitudes, as observed in cosmic-ray data.

In order to address this issue and continue with experimental data taking, the following plan was executed:

- 1. Once the BBS and SBS arms were in their final positions for a given configuration, cosmic data were taken with no magnetic field.
- 2. These data were used to gain-match the PMTs to a very high target signal amplitude (≥ 25 mV) so that no PMT signals were lost when the magnetic field was turned on.
- The BBS and SBS magnets were turned on at the strength needed for data taking, and more cosmic data was taken.
   The PMT gain-matching done during this process yielded HV settings that account for the fringe field.

Any time there was a change in experimental configuration, this process was repeated.

#### 5.2. Beam Calibrations

During data analysis of E12-09-019, the energy resolution of BBCal with only cosmic calibrations was evaluated using

H(e,e'p) events. We compared BBCal energy results to the scattered electron momentum found from the optics program for the BBS detector stack<sup>3</sup>, and we found that with just cosmic calibrations, the energy resolution was on the order of 10%, which was sufficient for running and commissioning but suboptimal for final results and analysis. This indicated a need for more rigorous energy calibrations.

To improve upon the resolution, the gain coefficients were calibrated again in the offline analysis using hydrogen target data. This was done by implementing a  $\chi^2$  minimization of the scattered electron energy as measured by BBCal and the electron reconstructed track momentum as measured using the tracking detectors. The following function was defined:

$$\chi^2 = \sum_{i=1}^{N} (E_e^i - E_{BBCal}^i)^2$$
 (5)

where N is the number of hydrogen target events within a given kinematic configuration,  $E_e^i$  is the reconstructed track momentum, and  $E_{BBCal}^i$  is the energy of a given BBCal cluster consisting of M PS and SH modules as defined by:

$$E_{BBCal}^{i} = \sum_{j=0}^{M} c_j A_j^{i} \tag{6}$$

where  $c_j$  is the ADC gain coefficient of the  $j^{\text{th}}$  module of the cluster, and  $A_j^i$  is the module's ADC pulse integral. This  $\chi^2$  function was then minimized with respect to the gain coefficients for each PS and SH block:

$$\frac{\partial \chi^2}{\partial c_j} = \sum_{i=1}^{N} \left( A_j^i - \sum_{k=0}^{M} \frac{A_j^i A_k^i}{E_e^i} c_k^i \right) = 0 \tag{7}$$

This equation results in 241 unique linear equations representing the 189 SH blocks and 52 PS blocks. This system of equation was solved to find the gain coefficients for all of the modules in BBCal.

In order to achieve the best BBCal energy calibration, we wanted to focus on scattered electron events within the experimental acceptance that had well-defined track momentum. The SBS track momentum calibration was optimized for elastic events [14]. However, we needed to balance focusing on elastic events with maintaining enough statistics for the blocks within the acceptance. We achieved this balance by placing loose cuts on the data to select for elastic events. This allowed us to look at primarily elastic events while also keeping statistics reasonable.

Furthermore, an active area cut was made on BBCal to exclude events for which the cluster center was on the outer edges of the SH layer, ensuring that the clusters used to calibrate BBCal energy were entirely contained within the calorimeter.

The quality of the energy calibration was confirmed by analyzing plots of the ratio of  $E_{BBCal}$ , the total calibrated energy deposited into BBCal for a given event, and p, the reconstructed

<sup>&</sup>lt;sup>3</sup>Relativistic electrons have E = p.

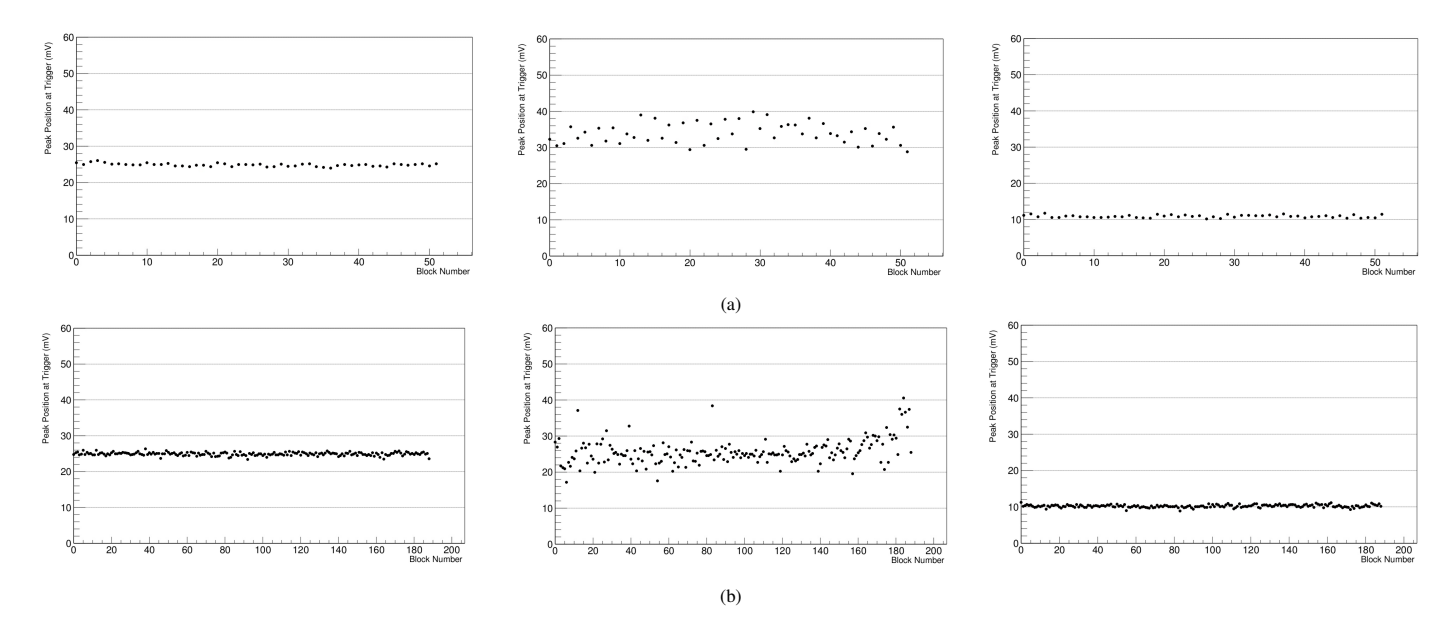
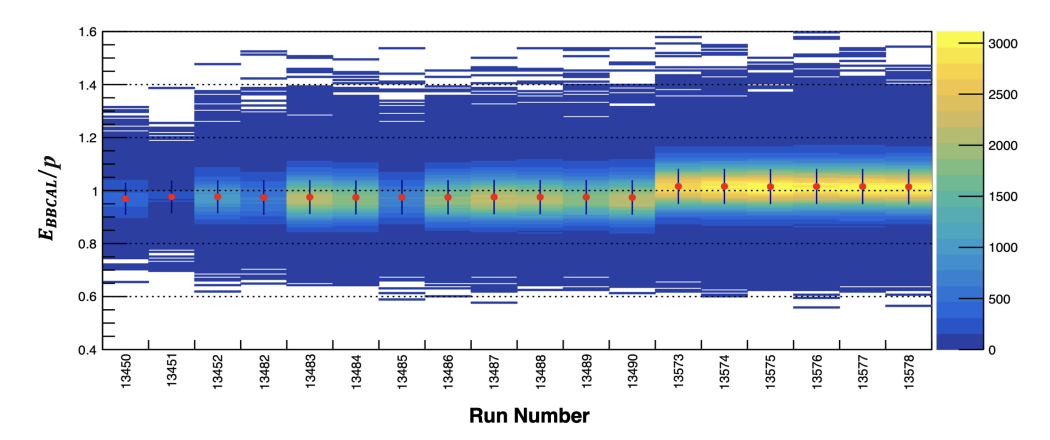
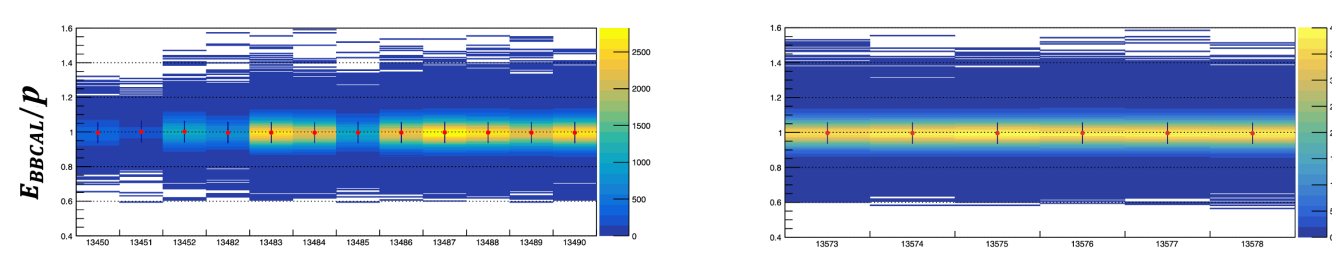


Figure 13: Mitigation of PS (a) and SH (b) PMT gain instabilities induced by stray magnetic fields from the SBS and BBS dipole magnets. Each panel shows the peak position of the cosmic-ray signal amplitude distribution as a function of block ID. Left panels: data from a cosmic-ray run taken with both magnets off, following initial gain-matching of the PMTs. Middle panels: data from a run taken with both magnets on, demonstrating the degradation of the gain-matching due to fringe fields. Right panels: data after re-gain-matching using the magnet-on cosmic-ray run, yielding uniform PS and SH amplitudes of approximately 10 mV. The target amplitude was chosen based on kinematic considerations to avoid saturation of the S/A modules.



(a) There is a clear shift between runs 13490 and 13573, and the E/p values on either side of this shift are not well aligned at one.



(b) The runs before the shift seen in 14a, calibrated separately so that their E/p values align at one.

(c) The runs after the shift seen in 14a, calibrated separately so that their E/p values align at one.

Figure 14: E/p versus run number for a given data set in which a shift can be seen. The red points represent the mean of the Gaussian fit on each E/p peak.

scattered electron track momentum. This E/p ratio should ideally be equal to one due to the relativistic nature of the scattered electrons. Fig. 15 shows that the energy of scattered electrons calibrated using cosmic data was not uniform, with a tail at higher energies, and was not as similar to the reconstructed

momentum as the energy of the scattered electrons calibrated by hydrogen data.

After initial energy calibrations were complete, the plots of  $E_{BBCal}$  over p were analyzed run-by-run to check for any possible deviations. Various small deviations were observed

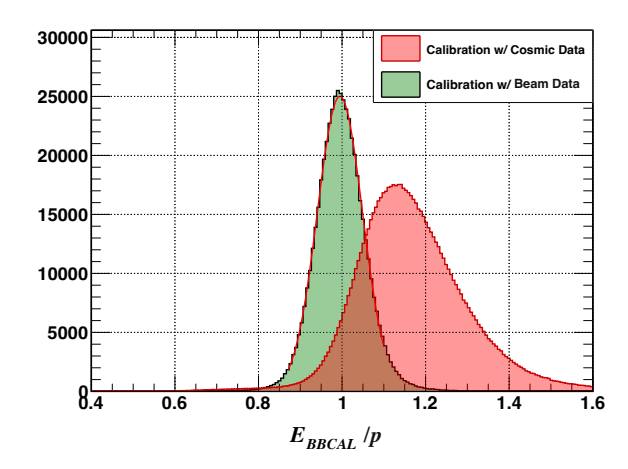


Figure 15: An example of an E/p ratio from E12-09-019. The red curve represents data calibrated using cosmic data, and the green curve represents data calibrated using beam data.

throughout individual kinematic configurations which were accounted for during calibrations. Subgroups of runs that had a significant shift compared to others in the same configuration were calibrated separately to generate their own sets of gain coefficients. As can be seen in Fig. 14, once the subgroups were separated and recalibrated, they each showed  $E_{BBCal}$  over p peaks centered at one.

#### 6. Timing Calibration

The leading-edge (LE) time of each BBCAL signal pulse was reconstructed directly from the fADC waveform samples using a simple linear interpolation between the two consecutive fADC samples occurring before and after the voltage reaches half of its maximum value on the rising edge of the pulse. For signals well above the software threshold for pulse-finding in the waveform, this algorithm is roughly equivalent to a constant-fraction discrimination, which minimizes time-walk effects in the reconstruction.

Slight non-uniformities in the signal processing circuitry, including but not limited to cable length variations, introduced timing offsets into the PMTs relative to the expected signal arrival times at each BBCal block, necessitating a calibration. Moreover, the sensitivity of the BBCal PMTs to the fringe fields of the SBS magnet required separate timing calibrations for different magnetic field settings.

BBCal ADC times were aligned to the BigBite timing hodoscope (see Section 1 and Fig. 1). Detailed descriptions of the hodoscope design and performance characteristics can be found in, e.g., [14]. The typical intrinsic hodoscope resolution after final calibrations was 200-300 ps throughout the SBS program, depending on experimental conditions. However, its effective resolution for time-of-flight measurement is degraded for higher-energy electrons due to the larger spread in both space and time of electromagnetic shower secondaries generated in the PS that contribute to the hodoscope signals. At the same time, the SH timing resolution improves as the electron

energy increases. At the highest electron energies (approaching 4 GeV) measured by BigBite during the SBS program, the SH timing resolution equals or even exceeds that of the hodoscope. The BBCal-hodoscope alignment was achieved via Gaussian fits to the distributions of the time differences between individual PS and SH ADC channels and the hodoscope mean cluster time, after the latter was corrected for electron time-of-flight variation within the BigBite acceptance and aligned to the accelerator RF signal.

As shown in Fig. 16, after alignment, the residual channel-to-channel variations in the BBCal-hodoscope time differences were small compared to the combined intrinsic resolution of the detectors. In Fig. 16, some channels in the periphery of the acceptance were not successfully calibrated due to insufficient statistics. For these channels, an offset was assigned based on an average of the nearest successfully calibrated neighboring channels, with somewhat mixed results. Manual, post hoc adjustments were made on some channels with poor data and/or fit quality as needed. For the most part, poorly-calibrated channels were outside the useful acceptance of the BBS anyway.

As can be seen in Fig. 16, the distributions of PS-hodoscope time differences are slightly skewed/asymmetric, even after alignment. This reflects a neglected spurious correlation between the PS ADC time and the horizontal position at which the electron track crosses the PS. Figure 17 shows an example of this correlation from E12-09-019 data. The observed correlation is suggestive of light propagation delay being the main physical mechanism; tracks crossing the PS blocks closer to the PMTs produce earlier signals. The magnitude of the effect (about 2 ns variation over the ~30-cm length of the blocks) is also qualitatively consistent with this interpretation, given the expected effective light propagation speed in lead-glass, accounting for the refractive index and the angular distribution of the Cherenkov radiation emitted by relativistic charged particles and shower secondaries.

One way of estimating the intrinsic time resolution of BB-Cal is to compare the SH and PS ADC times to the hodoscope (which in most cases has significantly better resolution) after final alignments. Figure 18 shows a representative example of the time difference distributions between the SH/PS and the hodoscope after final calibrations, for data from E12-09-019. The PS times shown in Fig. 18-bottom were corrected for the correlation shown in Fig. 17 before subtracting the hodoscope times. While the widths shown in Fig. 18 are determined by the combined resolution of the hodoscope and BBCal, they are mostly dominated by the BBCal timing resolution, as the estimated hodoscope resolution for this setting was 250 ps. The comparisons above suggest the typical BBCal time resolution is 0.4-0.5 ns.

# 6.1. ADC Time Shifts

Throughout data taking, there were occasional global timing shifts affecting the BBCal ADC signals (and those of other detectors) within a single kinematic due to various changes in the DAQ system settings. The solution for dealing with these shifts was simply to separately align subsets of the data within which the ADC times were constant. It was usually sufficient to apply

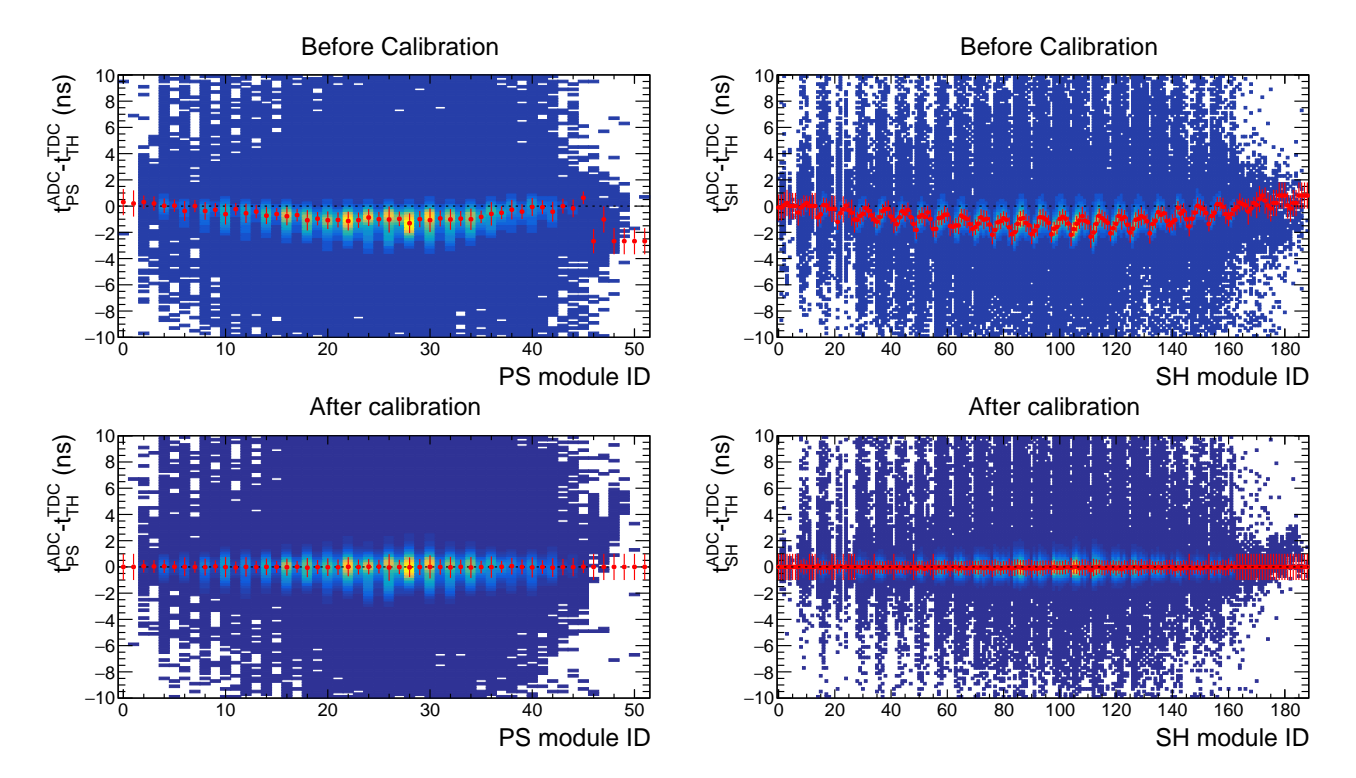


Figure 16: Time difference between TDC time in the scintillator hodoscope and ADC time in the PS (left) and SH (right) versus block number, before (top) and after (bottom) timing alignment. The red markers show the mean of a Gaussian fit to the peak in each channel's time difference distribution. The error bars in all four plots represent the standard deviation of the Gaussian fit, which serves as a measure of the resolution. In the bottom row, channels with insufficient statistics were arbitrarily assigned a mean of zero and a standard deviation of 1 ns for plotting purposes. See text for details.

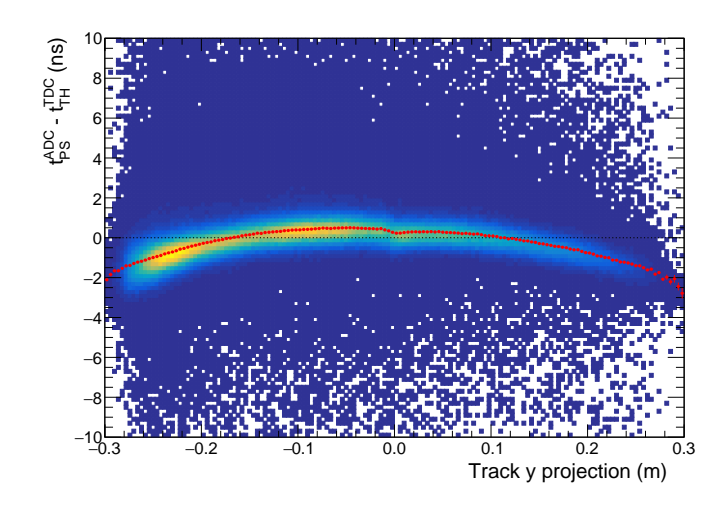


Figure 17: PS-hodoscope time difference versus the horizontal position of the track projection to the PS. Red markers show the approximate mean of the distribution at each position. Tracks crossing the PS closer to the PMTs give earlier arrival times as naively expected. The "kink" in the distribution near the center reflects the boundary between the left and right columns of the PS. Note that the direction of the *y* coordinate in this figure runs from small to large scattering angles; i.e., from left to right as viewed from downstream, when BigBite is on beam left.

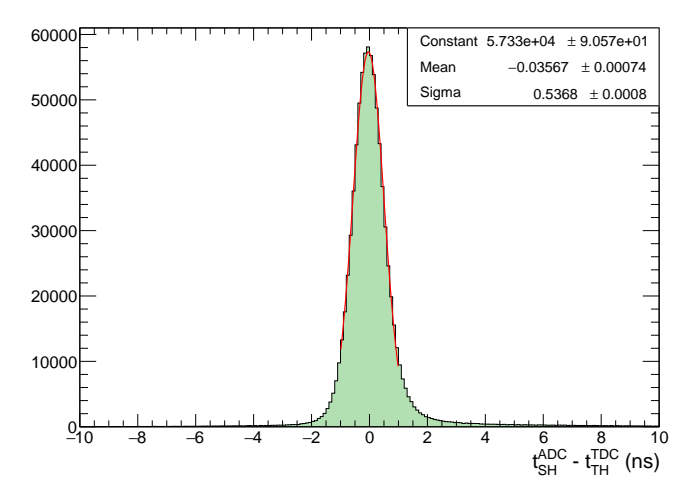
a single global offset to all fADC times within each subset to align all the data from any given kinematic setting.

There were also random, event-by-event timing shifts observed within individual runs. Some of these shifts were attributable to miscellaneous non-uniformities in the timing of trigger formation itself and the characteristics of the readout electronics, while others were introduced, apparently at random, by the trigger supervisor, affecting the timing of the detector signals from triggered events relative to the "Level 1 Accept" signal that causes the DAQ system to acquire an event, opening the "look-back" windows for each detector. Fortunately, these random event-by-event timing shifts were found to be perfectly correlated across all detectors, such that they did not negatively impact the analysis of relative timing between the various detector subsystems, including relative time-of-flight measurements and/or coincidence timing between the two spectrometer arms.

#### 6.2. Out-of-Time Hits in SH Clusters

Throughout data taking, double peaking was observed in plots of the time difference between the ADC time of hits in the primary block and in the secondary block of only SH clusters, as can be seen in Fig. 19.

These out-of-time hits were low energy, approximately 1% of the highest energy hit, and occurred when the secondary block was in a separate row from the primary block. Thus, the likely cause of these out-of-time hits is multiple scattering of low-energy events from the main electromagnetic shower. Likely



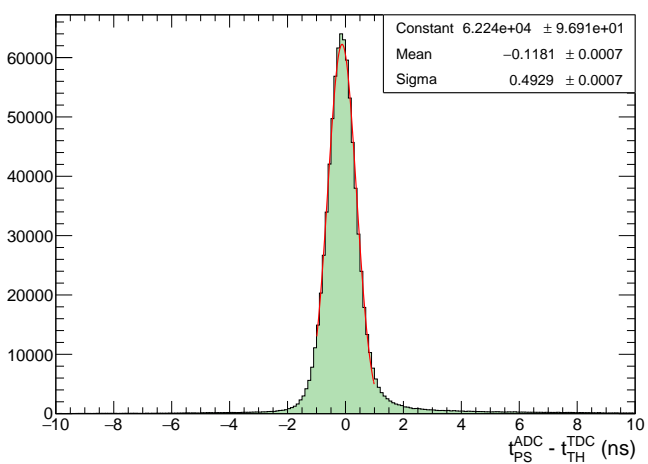


Figure 18: SH-hodoscope (top) and PS-hodoscope (bottom) time difference distributions after final calibrations, with Gaussian fits to estimate the resolution. The PS time has been corrected for the correlation with horizontal position shown in Fig. 17. Assuming 250-ps resolution for the hodoscope, the implied SH (PS) timing resolution is  $\sigma_{I} \approx 0.48(0.43)$  ns.

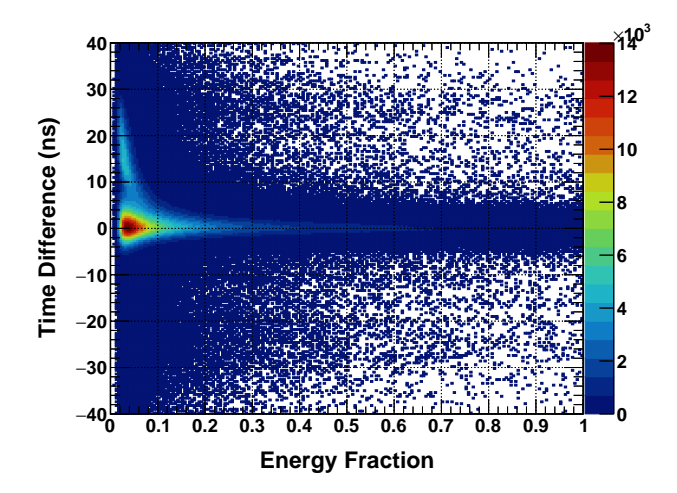


Figure 19: Correlation between the time difference of the secondary and primary blocks in a SH cluster and the ratio of the secondary block's energy to that of the primary, with low-energy out-of-time hits clearly visible.

the mu-metal between the SH rows increased the probability of multiple scattering, which is supported by the fact that out-of-time hits were only seen in the SH and were seen when the cluster spanned over two SH rows. We found that a simple  $\pm 10$  ns cut on the ADC time difference between primary and secondary blocks in a cluster not only got rid of the out-of-time hits, but also improved the energy resolution across all kinematic configurations.

#### 7. Simulation

Data analysis of SBS experiments requires a realistic simulation framework to accurately model relevant physics processes and detector effects. This framework comprises event generators that include relevant physics processes, a detailed Geant4-based geometry of the experimental setup—including the target and spectrometers [11], a C++ library that digitizes simulated events to emulate signal processing effects [15], and a reconstruction library that processes the resulting pseudo-raw data [12]. Together, these components enable direct and meaningful comparisons between simulated and experimental data.

Figure 20 shows an example comparison of the PS energy distribution from the E12-09-016 experiment, using  $^3$ He data at  $E'_e = 2.7$  GeV. The gray filled histogram represents the measured data, showing a broad peak from quasi-elastically scattered electrons and a narrow peak at low energy from MIPs. To simulate these features, quasi-elastically scattered electrons (orange curve) and negatively charged pions in the relevant momentum range (blue curve) were generated separately using the SBS simulation framework.

The simulation uses the following Geant4 physics lists: G4EmStandardPhysics for electromagnetic processes, G4HadronPhysicsFTFP\_BERT for hadronic interactions, G4DecayPhysics for particle decays, G4StoppingPhysics to accurately model energy loss and particle stopping, G4StepLimiterPhysics for step control, and G4OpticalPhysics to simulate Cherenkov light. The black curve, representing the sum of the orange and blue components, shows good agreement with the data across the full energy range, indicating a solid understanding of the detector response.

#### 8. Online Monitoring

For quality assurance, several parameters of BBCal were monitored frequently during production running to debug any issues that may arise in real time. Some of these plots for SH and PS included hit counts, pedestal values, ADC time (ns), and signal amplitude (mV) vs blockID. Cluster variables such as SH and PS cluster multiplicity, "best" cluster distributions, position of the "best" cluster (see Fig. 21), and energy of the "best" cluster were monitored. Correlations between SH and PS cluster energies (GeV) and BBCal cluster correlation plots with detectors in the SBS arm, such as HCal were also monitored during production running.

As mentioned in Sec. 3.1, the trigger sums were continuously monitored to have additional checks on data quality and trigger

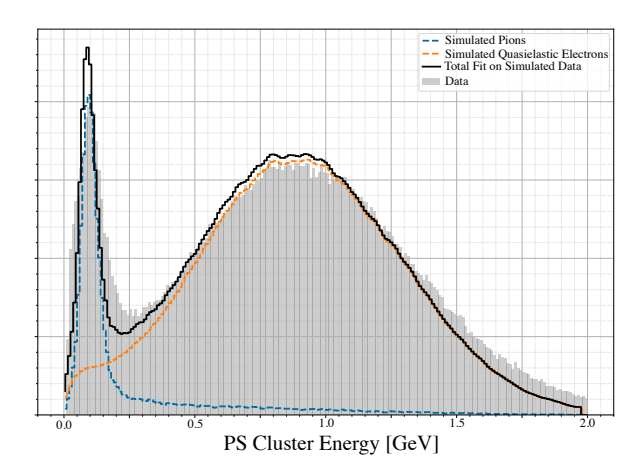


Figure 20: Data vs. simulation comparison of the PS energy distribution. The gray-filled histogram represents experimental data from the E12-09-016 experiment on a  $^3$ He target at  $E_e'=2.7$  GeV. The black curve represents the overall fit to the data, obtained by combining simulations of quasi-elastically scattered electrons (orange curve) and negatively charged pions (blue curve).

efficiency. These diagnostic plots include pedestal, ADC time, signal amplitude, TDC time vs trigger sum ID, trigger sums vs SH sums (shown in Table 2).

## 9. Calorimeter performance

#### 9.1. Energy Resolution

In order to quantify the energy resolution of BBCal, we looked at plots of the ratio of scattered electron energy as measured by BBCal over scattered electron momentum as measured by the tracking detectors; see Fig. 15. We define  $\sigma_{E'}/E'_e$ , the standard deviation of the Gaussian fit to the  $E_{BBCal}/p$  peak, as the energy resolution of the calorimeter. Fig. 22 shows the energy resolution as a function of the central elastic electron energy, with the values shown in Table 4. The data have been fitted using

$$\frac{\sigma_{E'}}{E'_e} = \frac{(3.9 \pm 0.1)}{\sqrt{E'_e}}\% + (3.4 \pm 0.2)\%$$
 (8)

which can be compared to the resolution fit equation found in [7].

The first term in Eqn. 8 is a stochastic term that accounts for sampling fluctuations [20]. The second term is a constant term that accounts for inhomogeneities in the detector they may arise from calibrations or geometry. This constant term also gives an idea of how good of a resolution we can possibly achieve. As the electron energy increases, we reach a lower limit on our energy resolution of approximately 3.4 %. There is often a third term in standard energy resolution fits that accounts for noise in

Table 4: BBCal energy resolution values for different kinematic points measured during E12-09-019.  $E_{\text{beam}}$  is the electron beam energy,  $E'_e$  is the central scattered electron energy,  $Q^2$  is the central  $Q^2$ , and  $\sigma_{E'}/E'_e$  is the measured BBCal energy resolution.

E <sub>beam</sub> (GeV)	$E'_e$ (GeV)	$Q^2 (\text{GeV/c})^2$	$\frac{\sigma_{E'}}{E'_e}$ (%)
4.0	1.6	4.5	$6.415 \pm 0.020$
6.0	2.0	7.4	$6.252 \pm 0.053$
3.7	2.1	3.0	$5.997 \pm 0.032$
7.9	2.7	9.9	$5.796 \pm 0.051$
9.9	2.7	13.6	$6.429 \pm 0.165$
6.0	3.6	4.5	$5.419 \pm 0.025$

the signal. This noise term was excluded in Eqn. 8 due to the small energy range in which BBCal was used in SBS.

The weighted average of all of the energy resolution values shown in Fig. 22 is approximately 6.2 %, which is our final quoted resolution in the relevant energy range.

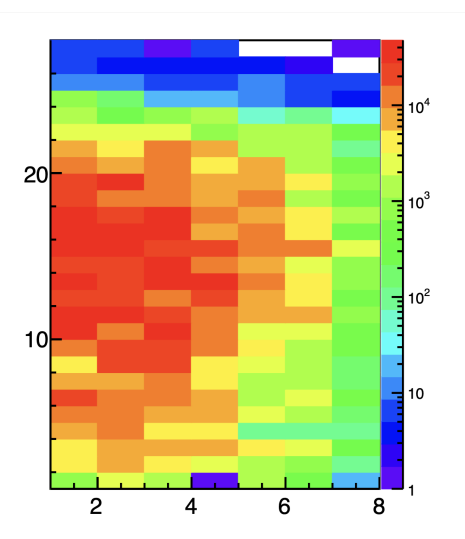
## 9.2. Timing Resolution

In section 6, the time difference between BBCal and the Big-Bite timing hodoscope was used as a proxy for the BBCal timing resolution, suggesting a resolution of 0.4-0.5 ns. Another way to estimate the BBCal time resolution is by comparing the shower and preshower timing, or examining the time differences between neighboring blocks within a given BBCal cluster. For the scattered electrons in the SBS experiments, it is naively expected that two neighboring blocks within a cluster should fire at approximately the same time, so the difference between the ADC times of these two blocks should be dominated by the timing resolution of the calorimeter. Thus, the time differences between blocks within a cluster, or between shower and preshower blocks, serve as a useful cross-check of the estimates based on comparisons to the hodoscope presented in section 6.

Figure 23 shows two time difference spectra based on comparisons of different BBCal signals. First, the time difference between the highest-energy blocks in the preshower and shower clusters shows a width of approximately 0.5 ns, more or less consistent with the comparisons to the timing hodoscope shown in section 6. Secondly, the time difference between secondary blocks and the primary block in the shower cluster shows a larger width of about 0.86 ns. This is attributable to the generally poorer timing resolution for small signals in the periphery of shower clusters, as compared to the primary block, which tends to give the best timing resolution. We can also make such comparisons for primary and secondary blocks in the preshower; however, the majority of preshower clusters consist of exactly one block (see figure 10), except at the boundaries between rows and columns.

Events selected for the analysis shown in Fig. 23 were elastically scattered electrons from hydrogen, with an average energy of 1.6 GeV. At this incident electron energy, the total energy deposit in BBCal is divided fairly evenly between the shower and the preshower. The electrons were required to deposit at least 0.2 GeV in both the shower and preshower, and to have an

<sup>&</sup>lt;sup>4</sup>The  $Q^2 = 13.6 \text{ GeV}^2$  kinematic point in E12-09-019 was redundant with the  $Q^2 = 9.9 \text{ GeV}^2$  point, both having a central elastic electron energy of 2.7 GeV, as seen in Table 4, and the higher  $Q^2$  point had very low statistics in its calibration data. For these reasons, we have omitted this point in our energy resolution analysis.



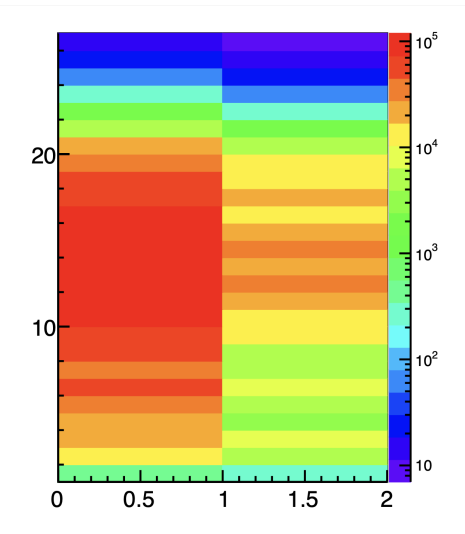


Figure 21: An example of the position of best cluster in the SH (left) and PS (right) detectors as shown by the online monitoring software. Both plots have the same axes: horizontal is detector column ID and vertical is detector row ID. The color scale shows the number of hits. The plot on the left shows the SH and on the right is the PS.

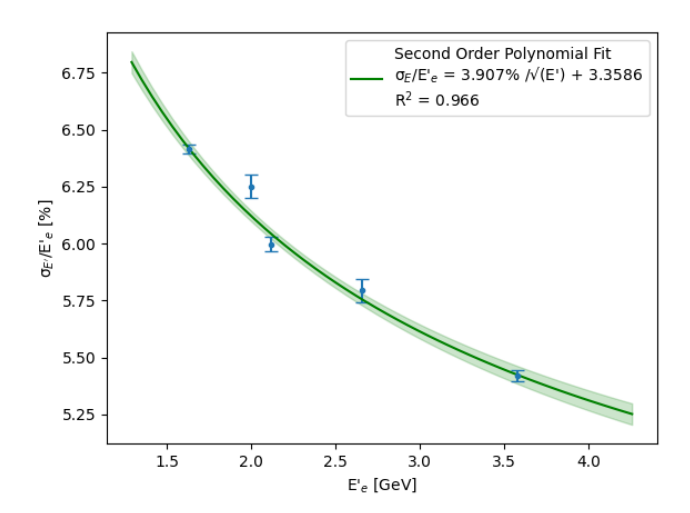


Figure 22: Energy resolution versus central elastic electron energy for kinematic points in E12-09-019. There is a  $1-\sigma$  error band on the fit.<sup>4</sup>

E/p ratio between 0.7 < E/p < 1.3 (see Fig. 15). The energy deposition in the secondary blocks was also required to be at least 20% of the primary block's energy deposit and only secondary blocks immediately adjacent to the primary block were considered. No additional requirements were imposed on either the primary or secondary blocks' energies. As such, many hits with relatively low energies are included in the comparison, explaining its larger width, consistent with the energy dependence of time differences shown in Fig. 19.

Higher incident electron energies and/or higher thresholds on the individual shower block energies lead to smaller time differences between primary and secondary blocks in shower clusters. Apart from the significantly delayed "out-of-time" hits in the shower clusters, as seen in Fig. 19, there is no evidence for a significant "time-walk" effect at low energies with the standard reconstruction algorithm for leading-edge times; instead, it seems the time resolution for individual shower blocks is sim-

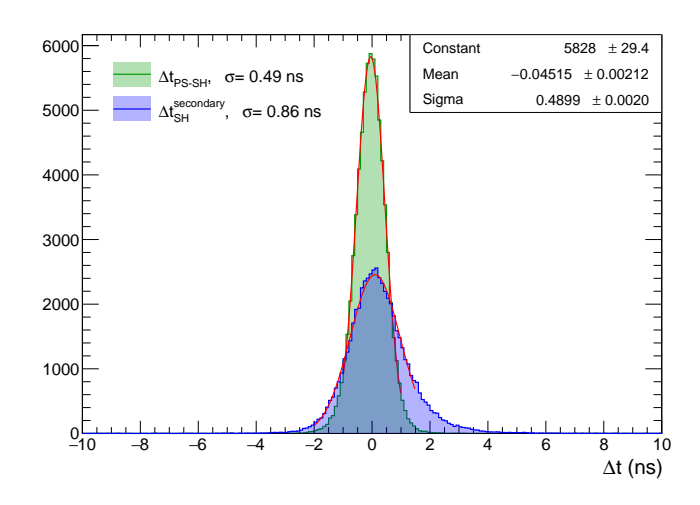


Figure 23: Time difference between highest-energy preshower and shower blocks (green) and between secondary and primary blocks in the shower cluster (blue), for data from E12-09-019. These comparisons use elastically scattered electrons with an average energy of approximately 1.6 GeV. See text for details.

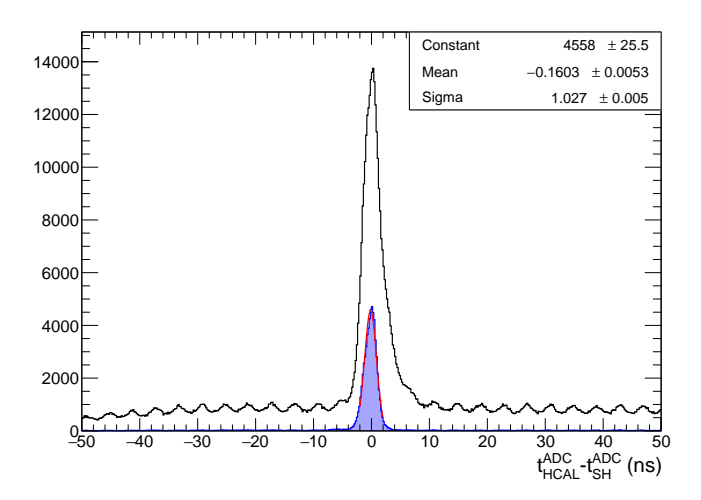


Figure 24: Difference between HCAL and BBCal ADC times. The black histogram shows all events with a good electron in BigBite, with real coincidence peak and accidental background showing the 4-ns beam bunch spacing of CE-BAF used during E12-09-019. The blue shaded histogram shows the same distribution for elastically scattered electrons from hydrogen, selected by a cut on the reconstructed virtual photon-nucleon invariant mass W, illustrating the suppression of accidental coincidences and the 1-ns coincidence time resolution, dominated by HCAL.

ply degraded for energy depositions below about 200 MeV. In practice, the overall effective timing resolution for BBCal, taking the highest-energy blocks in both the shower and preshower, was about 0.4-0.5 ns as suggested by the comparison to the hodoscope.

During the SBS experiments, the coincidence time between when BBCal measured an event and when the hadron calorimeter (HCAL) measured an event was used to define in-time events of interest. While some of the experiments used a single-arm trigger based on BBCal alone, others used a coincidence between BBCal and HCAL. While this paper will not go into detail regarding the hadron calorimeter, the resolution of this coincidence time was extremely important for the suppression of accidental and inelastic backgrounds. The resolution of coincidence time was typically dominated by HCAL, which had a resolution of approximately 0.8-1 ns. Fig. 24 shows a typical example of the HCAL-BBCal coincidence time distribution, before and after elastic event selection. The combined resolution of BBCal and HCal was sufficient to resolve the 4-ns beam bunch spacing in the accidental coincidence distribution.

#### 9.3. Position Resolution

The position resolution of BBCal can be estimated using the highly precise tracking system which sits upstream of the PS layer. The design of the PS layer naturally leads to poor position resolution in the horizontal direction. This was not an issue in SBS because, as mentioned in Sec. 2, BBCal was only used as a starting point for the tracking algorithm, and only the SH position was used. However, due to the high event rate seen on the GEMs, it was important that BBCal had a sufficient position resolution such that BBCal could be used to define an initial search region for the tracking reconstruction.

The tracking system in E12-09-019 as a whole has a position resolution of approximately 70  $\mu$ m, so we can compare the positions of hits as measured by BBCal to those measured by the tracking system to get a value which describes the resolution in the SH layer. The position of a hit in the SH is defined as the energy-weighted centroid of the cluster corresponding to that hit. These hit values can be compared to those found in the tracking system, as seen in Fig. 25.

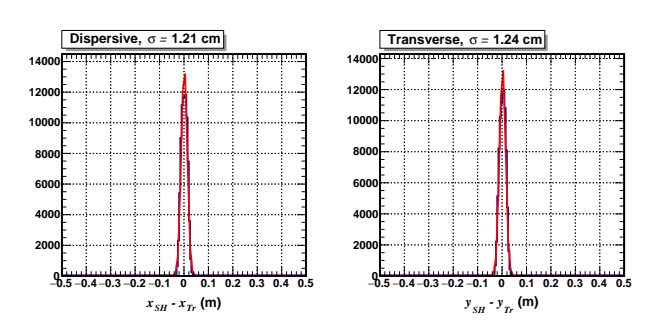


Figure 25: The difference in position in the dispersive (left) and non-dispersive (right) directions as measured by the BBCal SH layer and the tracking system for scattered electrons using E12-09-019 data.

Given the use of BBCal to gain an initial position estimate for track reconstruction, a resolution of approximately 1.2 cm was more than sufficient.

## 10. Summary

A new electromagnetic calorimeter, BBCal, was constructed, installed, maintained and calibrated for the SBS form factor series of experiments in experimental Hall A at Jefferson Lab. The calorimeter met its desired goals in terms of energy, position, and timing resolution. Overall, BBCal performed reliably and was invaluable for the success of the SBS physics program.

## 11. Acknowledgments

We acknowledge the SBS collaboration who helped support the BBCal team and the JLab Hall A technical staff for providing outstanding support throughout the duration of the detector operation. We also thank David Armstrong for providing valuable feedback. This material is based upon work supported by the U.S. Department of Energy, Office of Science, Office of Nuclear Physics under contract DE-AC05-06OR23177 under which the Southeastern Universities Research Association (SURA) operates the Thomas Jefferson National Accelerator Facility for the United States Department of Energy. This work was also supported in part by the National Science Foundation contract PHY-2412825, and by the US Department of Energy Office of Science, award ID DE-SC0021200.

#### References

[1] P. A. Adderley et al. "The Continuous Electron Beam Accelerator Facility at 12 GeV". In: Phys. Rev. Accel. Beams 27 (8 Aug. 2024), p. 084802. DOI: 10.1103/PhysRevAccelBeams. 27.084802. URL: https://link.aps.org/doi/10.1103/PhysRevAccelBeams.27.084802.

- [2] G. A. Akopdzhanov et al. In: Nucl. Instrum. Methods 161 (1979), p. 247. URL: https://www.sciencedirect.com/science/article/pii/ 0029554X79903914
- [3] H. Avakian et al. In: *Nucl. Instrum. Methods A* 378 (1996), p. 155. DOI: 10.1016/0168-9002(96)00443-3.
- [4] K. Ackerstaff et al. In: Nucl. Instrum. Methods A 417 (1998), p. 230. arXiv: hep-ex/9806008.
- [5] M. Y. Balatz et al. In: Nucl. Instrum. Methods A 545 (2005), p. 114. DOI: 10.1016/j.nima.2005.01.328.
- [6] R. G. Astvatsaturov et al. In: Nucl. Instrum. Methods 107 (1973), p. 105.URL: https://www.sciencedirect.com/science/article/pii/0029554X73900189.
- [7] H Avakian et al. "Performance of the electromagnetic calorimeter of the HERMES experiment". In: Nuclear Instruments and Methods in Physics Research Section A: Accelerators, Spectrometers, Detectors and Associated Equipment 417.1 (1998), pp. 69-78. ISSN: 0168-9002. DOI: https://doi.org/10.1016/S0168-9002(98)00540-3. URL: https://www.sciencedirect.com/science/article/pii/S0168900298005403.
- [8] H. Avakian et al. "Performance of F101 radiation resistant lead glass shower counters". In: Nuclear Instruments and Methods in Physics Research Section A: Accelerators, Spectrometers, Detectors and Associated Equipment 378.1 (1996), pp. 155-161. ISSN: 0168-9002. DOI: https://doi.org/10.1016/0168-9002(96)00443-3. URL: https://www.sciencedirect.com/science/article/pii/ 0168900296004433
- [9] M.Y. Balatz et al. "The lead-glass electromagnetic calorimeter for the SELEX experiment". In: Nuclear Instruments and Methods in Physics Research Section A: Accelerators, Spectrometers, Detectors and Associated Equipment 545 (June 2005), pp. 114–138. doi: 10.1016/j.nima. 2005.01.328.
- [10] G. D. Cates, S. Riordan, and B. Wojtsekhowski. Measurement of the Neutron Electromagnetic Form Factor Ratio  $G_E^n/G_M^n$  at High  $Q^2$ , JLab experiment E12-09-016. 2009.
- [11] SBS Collaboration. g4sbs. Dec. 2013. url: https://github.com/ JeffersonLab/g4sbs.
- [12] SBS Collaboration. SBS-Offline: Reconstruction and Analysis Code for superbigbite (SBS) experiments. June 2016. URL: https://github.com/JeffersonLab/SBS-offline.
- [13] Leo R. Dalesio et al. "The Experimental Physics and Industrial Control System architecture: Past, present, and future". In: *Nucl. Instrum. Meth.* A 352 (1994), pp. 179–184. DOI: 10.1016/0168-9002(94)91493-1.
- [14] Provakar Datta. "Precision Measurements of the Neutron Magnetic Form Factor to High Momentum Transfer using Durand's Method". PhD thesis. Univ. of Connecticut, Storrs, CT (United States), Connecticut U., 2024. arXiv: 2508.18158 [nucl-ex].
- [15] Eric Fuchey, Juan Carlos Cornejo, and Andrew Puckett. Mar. 2018. URL: https://github.com/JeffersonLab/libsbsdig.
- [16] Jefferson Lab data acquisition group. FADC250 User's Manual. 2013. URL: https://www.jlab.org/Hall-B/ftof/manuals/ FADC250UsersManual.pdf.
- [17] Photonis. Photomultiplier Tube Basics. 2002. URL: https://psec.uchicago.edu/library/photomultipliers/Photonis\_PMT\_basics.pdf.
- [18] X. Qian et al. "Single Spin Asymmetries in Charged Pion Production from Semi-Inclusive Deep Inelastic Scattering on a Transversely Polarized <sup>3</sup>He Target". In: *Phys. Rev. Lett.* 107 (2011), p. 072003. DOI: 10. 1103/PhysRevLett.107.072003. arXiv: 1106.0363 [nucl-ex].
- [19] S. Riordan et al. "Measurements of the Electric Form Factor of the Neutron up to  $Q^2=3.4GeV^2$  using the Reaction  ${}^3He^{->}(e^{->},e'n)pp$ ". In: Phys. Rev. Lett. 105 (2010), p. 262302. DOI: 10.1103/PhysRevLett. 105.262302. arXiv: 1008.1738 [nucl-ex].
- [20] Isabelle Wingerter-Seez. Calorimetry: Concept & Examples, ESIAP Lecture 1. [Accessed 2025]. 2016.

- [21] B. Wojtsekhowski, E. Fuchey, and S. Alsalmi. Measurement of the Two-Photon Exchange Contribution to the Electron-Neutron Elastic Scattering Cross Section, JLab experiment E12-20-010. 2020.
- [22] B. Wojtsekhowski, D. Hamilton, and B. Quinn. Precision Measurement of the Neutron Magnetic Form Factor up to Q<sup>2</sup>=18.0 (GeV/c)<sup>2</sup> by the Ration Method, JLab experiment E12-09-019. 2009.
- [23] B. Wojtsekhowski et al. Measurement of the Ratio GEn/GMn by the Double-polarized 2H(e,e'n) Reaction, JLab experiment E12-17-004. 2017.
- [24] B. Wojtsekhowski et al. Polarization Transfer in Wide-Angle Charged Pion Photoproduction E12-20-008. 2007.